

Reprint from ApJ, 557, 637–645, 2001.

© 2001. The American Astronomical Society. All rights reserved.

Mid Infrared Spectral Energy Distribution of NGC 1068 with $0''.1$ Spatial Resolution ¹

Daigo Tomono², Yoshiyuki Doi, Tomonori Usuda, and Tetsuo Nishimura

Subaru Telescope, National Astronomical Observatory of Japan, Hilo, HI 96720

tomono@mpe.mpg.de

ABSTRACT

The central region of the Seyfert 2 galaxy NGC 1068 is imaged in the mid infrared (MIR) using the Mid-Infrared Test Observation System on the 8.2 m Subaru Telescope. The oversampling pixel scale associated with shift-and-add method shows $0''.1$ resolution images with a high dynamic range after deconvolution. Along with an extended structure at a position angle (P.A.) of -10° with higher surface brightness, another structure extends wider with lower surface brightness at a P.A. of 20° . The central peak elongates north-south with FWHM of $0''.3 \times 0''.2$. Spectral energy distribution (SED) of the central peak is fitted to have the silicate absorption feature of $\tau_{9.7\mu m} = 0.9 \pm 0.3$. This is half of the absorption expected from the near-infrared (NIR) feature of carbonaceous dust. This suggests a temperature gradient of the absorbing dust along the line of sight. Another possibility, which is not distinguishable here, is the size distribution of dust different from our Galaxy. Intrinsic luminosity of emission from the central peak is 3×10^{37} W. The SED shows a hint of the poly aromatic hydrocarbon (PAH) emission features. Although a high spatial resolution MIR spectrum is required, it suggests that the PAH carriers near the active galactic nuclei (AGNs) are sheltered from the high-energy emission from the AGNs and the AGNs have nuclear starbursts. For the NIR disklike structures, no counterparts are detected in the MIR. The nature of the structures remains unclear.

Subject headings: galaxies: active, galaxies: individual (NGC 1068), galaxies: nuclei, galaxies: Seyfert, infrared: galaxies

NGC 1068

²Current address: Max-Planck-Institut für extraterrestrische Physik, Giessenbachstrasse 1, 85748 Garching, Germany.

¹Based on data collected at Subaru Telescope, which is operated by the National Astronomical Observatory of Japan.

1. Introduction

NGC 1068 is the prototype of Seyfert 2 galaxies (Antonucci 1993). Antonucci & Miller (1985) detected broad emission lines in polarized light and confirmed that it has a Seyfert 1 type active galactic nucleus (AGN) in the center of the galaxy. The Seyfert 2 AGN is obscured by a dust torus. There have been a number of observations trying to detect the plausible torus that has a key to explain the differences between Seyfert 1 and Seyfert 2 nuclei. For example, adaptive optics (AO) images by Marco & Alloin (2000) in the L and M bands show disklike structures in the east and west of the near infrared (NIR; 1–5 μm) peak of NGC 1068. However, no counterparts have been observed in the mid infrared (MIR; 8–13 μm and $\sim 20 \mu\text{m}$), which the wavelength emission from the dust torus would peak. MIR spectra of NGC 1068 and other AGNs have shown the silicate absorption feature at 9.7 μm . This probably originates in dusty regions relatively close to the central source (Roche et al. 1984, 1991). When assessing the absorption, care must be taken because the infrared emitting region might have a spatial structure and therefore might contaminate the absorption feature toward the central source.

The advent of the 8 m class telescopes is expected to generate higher than ever angular resolution images in the MIR. Bock et al. (2000) observed NGC 1068 using the 10 m Keck II telescope with a pixel scale of $0''.138 \text{ pixel}^{-1}$. Using four filters in the MIR, they imaged spatial distribution of silicate absorption and interpreted that the northern elongation from the central peak is reprocessed radiation from the AGN, which is strongly beamed. The direction of the elongation is different from that in the MIR images of a wider field of view (FOV) by Braatz et al. (1993) and Marco, Alloin, & Beuzit (1997).

Using the Mid-Infrared Test Observation System (MIRTOS), we observed NGC 1068 to clarify the nature of the disklike structures imaged in the NIR and the difference of elongation in the MIR images. The 8.2 m Subaru Telescope provides us spatial resolution in the MIR comparable with that of the NIR AO images. The shift-and-add (SAA) method delivers diffraction-limited point-spread function (PSF) in the MIR. The pixel scale of the MIRTOS is small enough for image reconstruction methods such as deconvolution. Six filters are used in the 10 μm band along with an 18.5 μm filter to measure the silicate feature as well as the polycyclic aromatic hydrocarbon (PAH) band strengths.

The remainder of the paper is organized as follows: the observation procedures are discussed in § 2; data reduction procedures used to obtain the deconvolved images are discussed in § 3; the resulting data is presented in § 4; in § 5, the MIR radiation from the central peak is compared with the observations in other wavelengths; finally, § 6 contains a summary of our results. NGC 1068 is at $z = 0.0038$ (Bottinelli et al. 1990); $1''$ corresponds to 72 pc when $H_0 = 75 \text{ km s}^{-1} \text{ Mpc}^{-1}$.

2. Observations

Observations of NGC 1068 were made on 1999 December 31, 2000 January 9, and January 18 UT. We used the MIRTOS mounted at the Cassegrain focus of the 8.2 m Subaru Telescope.

MIRTOS is constructed for high angular resolution imaging employing the SAA method to fully extract the diffraction-limited angular resolution of the telescope. SAA is a method that shifts snapshot images to cancel the image motion from the atmospheric perturbation before co-adding the images. MIRTOS combines an MIR camera and an NIR camera that take simultaneous images in the same field. The MIR camera has an SBRC (now Raytheon) Si:As array with 320×240 pixels. Its FOV of $21'' \times 16''$ is provided by a pixel scale of $0''.067 \text{ pixel}^{-1}$. The pixel scale matches $\lambda/3D$ at $\lambda = 8 \mu\text{m}$ for $D = 8.2 \text{ m}$ and produces enough spatial sampling for deconvolution. The NIR camera can be used to obtain a reference point source for the SAA method. Sensitivity in the NIR is higher than in the MIR. Therefore, the image motion by the atmospheric perturbation can be measured even with the short integration time that is limited by the timescale of the image motion. It has an SBRC InSb array with 256×256 pixels. The pixel scale of $0''.028 \text{ pixel}^{-1}$ is small enough to detect the image motion. It provides an FOV of $7'' \times 7''$. As a beam splitter, a long pass interference filter is used to reflect the NIR light while passing through the MIR light. To adjust the optical axes of the two cameras to that of the telescope, the beam splitter and a flat-folding mirror can be moved in the cryostat. The MIR camera takes images with one of six filters from 7.7 through $12.3 \mu\text{m}$ or an $18.5 \mu\text{m}$ filter while the NIR camera images in the *J*, *H*, or *K*-bands. Reflective optics are used in both cameras with a common CdTe dewar entrance window. Details about MIRTOS are explained in Tomono (2000) and Tomono, Doi, & Nishimura (2000).

Filters used for this work are listed in Table 1. Because the target is bright enough, the SAA method was applied using NGC 1068 itself as the reference in the MIR and in the NIR separately. The integration time of each frame was made shorter than 0.1 s so that the image motion does not blur the images. Secondary mirror chopping was not ready at the time of the observations. Instead, we performed nodding observations. Integration for a nodding set was repeated as follows:

1. Accumulate short exposure frames on the target in the on-source field. In a duration of 3.0 s, MIR frames and NIR frames are integrated simultaneously. For the MIR, a sequence of 96 frames of 0.031 s integration time is acquired consecutively. For the NIR, integration time was 0.094 s for each of consecutive 32 frames.
2. Nod the telescope to the offset field.
3. Observe the blank sky in the offset field. (The source could be in the offset field.)
4. Nod the telescope back to the on-source field.

Through all the observations, the sky was photometric. Total time for each nodding cycle was typically 180 s.

For NGC 1068, most of the nodding sets were taken with the offset field at 30' north of the on-source field. On January 18, after quick reduction of some of the data that had been taken, it was confirmed that there is no significant radiation detected in the MIR around the core of NGC 1068. Therefore, some nodding sets were taken with the offset field at 8'' east of the on-source field so that both fields integrated the target in the MIR. Table 2 shows number of nodding sets taken on each night. For the observation on January 18, the nodding pairs with 8'' offset are counted as two sets.

The PSF reference sources were observed before or after the observation of NGC 1068 in each night. Table 3 shows the number of nodding sets taken for the PSF references. Typical nodding offset was 7'' east for the MIR and 3'' west for the NIR. All the nodding pairs are counted twice because the source was integrated in both the on-source field and the offset field. We did not have a chance to observe a PSF reference source in 18.5 μm on January 9. As a substitution, β And, observed on January 18, is used as the PSF reference to reconstruct the image. The SAA images of NGC 1068 are essentially the same for the two nights. For some nights, we also observed other point sources. To check deconvolution reliability, these data are processed in the same way as for the NGC 1068 data. Table 4 shows the number of nodding sets taken for the deconvolution test sources.

For flux calibration, data with lower time resolution are also used along with those used for the SAA method. These data were obtained in the process of pointing the telescope to the reference sources. The frame rate was the same for the SAA data, but the frames were co-added before being transferred to the host computers so that the transfer time was reduced. Table 5 shows the number of nodding sets taken for the flux reference stars. The brightness of the MIR reference star β And is taken from Cohen et al. (1995); the brightness of α CMa is taken from Tokunaga (1984), as well as that of α Ari from Rieke et al. (1985). K -band flux of GJ 105.5 and HD 40335 are taken from Elias et al. (1982).

3. Data reduction

3.1. Sky Subtraction and Shift-and-Add

The images are co-added in the following procedure. First, the foreground emission from the sky and the telescope is subtracted from every frame. Frames in the nodding pair are averaged to make the sky frame. Next, the SAA method is applied on the images. Images in a nodding pair are co-added by shifting them to cancel the movement of the images. The peak position of the object in each frame is detected after convolving the frame with the Airy pattern to minimize the noise. Afterwards, the images are averaged for each night taking the airmass difference into account. The 2.1, 11.7, and 12.4 μm images of NGC 1068 were taken with a wide range of air-mass for some nights. We use them to estimate the air-mass dependency of the signal. Air-mass dependencies at 11.7 and 12.4 μm were essentially the same. Because some of the data are taken at air mass as

large as 1.5, the signals are corrected assuming the estimated air-mass dependency. We estimate that the brightness conversion has 10% of uncertainty in the air-mass correction. The averaged images for different nights are compared and are confirm that surface brightness and shape are in a good agreement. Finally, the images are averaged over all the observation nights. Figure 1a shows the resultant SAA image in $11.7 \mu\text{m}$, for example.

3.2. Deconvolution

The SAA image in Figure 1a elongates to a position angle (P.A.) of -10° . The elongation is wider in the north than in the south. The $10 \text{ Jy arcsec}^{-2}$ contour spreads to the east by north of the central peak. The entire structure elongates from the north by east to the south by west. To look into the emission structures, image reconstruction methods are employed. Two of the image reconstruction methods, the Lucy-Richardson method (Lucy 1974) and the maximum entropy method (MEM; Cornwell & Evans 1985) are applied using the IRAF package³. The Lucy-Richardson method ended with the χ^2 ranging from 1 to 2 after 20 or less iterations. For the MEM, number of iteration was limited to 110. Again, resultant images for different nights are compared and confirm that they have essentially the same morphology. Moreover, the Lucy-Richardson images and the MEM images show the same structures, although the MEM images show more structures with high spatial frequency. The high spatial frequency structures are probably artifacts because they differ from night to night. Hereafter, the Lucy-Richardson deconvolved images are used.

Figure 1 shows the effect of deconvolution for the $11.7 \mu\text{m}$ image, starting with the image resulting from the SAA method in Figure 1a. Using the PSF in Figure 1b, the Lucy-Richardson deconvolution resulted in the image shown in Figure 1c. Figure 2 shows the deconvolved images of NGC 1068 in other wavelengths. The deconvolved image of the deconvolution test star is shown in Figure 1d. There are three pointlike structures around the star at the distance where the first diffraction ring would be. Different rotation angles of the instrument derotator may have caused the PSF difference. Thus, structures around the central peak of NGC 1068 at the distance of the artifact may be contaminated. As the images of NGC 1068 are taken with different rotator angles, influence of the artifactual structure in the deconvolved image should be less than that for the deconvolution test star.

The structures seen in the SAA image are more prominent in the deconvolved images. Except for the 2.1 and $7.7 \mu\text{m}$ images, spatial resolution of the images is the same in Figure 2. At $2.1 \mu\text{m}$, spatial resolution of the image is limited by the seeing. As for the $7.7 \mu\text{m}$ image, the cause of the difference is not clear.

³IRAF is distributed by the National Optical Astronomy Observatories, which are operated by the Association of Universities for Research in Astronomy, Inc., under cooperative agreement with the National Science Foundation.

3.3. Registration of the Central Peak

To compare the MIR structures with those in other wavelengths, images from other observations are overlaid on the MIR image. Braatz et al. (1993) measured relative position of the peak of NGC 1068 at $12.4 \mu\text{m}$ and in optical continuum. Between the K and I bands, Marco et al. (1997) measured relative position of the peaks. The positions of the $12.4 \mu\text{m}$ peak and the K -band peak agrees within the precision of the measurements. From our simultaneous observation in the K band and in the MIR, the peak of NGC 1068 in the two bands is measured to be at the same position with an accuracy of $\pm 0''.3$. The accuracy was limited by the gear backlash on the movable beam splitter. This will be improved in future observations. Braatz et al. (1993) also found that the $12.4 \mu\text{m}$ peak is consistent with the apex of the [O III] ionization cone (Evans et al. 1991). Hereafter, the MIR peak and the K -band peak are assumed to be at the position of the AGN.

Using the measurement of the K -band peak position (Marco et al. 1997) and the optical peak position in the [O III] image (Evans et al. 1991), the [O III] emitting clouds are registered on Figure 1c. It also illustrates the positions of the 5 GHz components (Gallimore, Baum, & O’Dea 1996) with the S1 component, which are most likely at the AGN, overlaid on the MIR peak. Moreover, peak positions of the NIR disklike structures (Marco & Alloin 2000) are shown in the figure.

4. Results

4.1. The Central Peak

To investigate the spatial distribution of dust around the AGN, the spatial extent of the central peak is measured and flux from the central peak is fitted by a model of a modified graybody absorbed by the silicate feature. As described in §3.3, the K -band peak and the MIR peak coincides with each other with the accuracy of ± 0.3 arcsec. Moreover, the infrared peak is at the position where the AGN and the dust torus reside.

4.1.1. Flux Measurement

An elliptical Gaussian is fitted on the central peak in the deconvolved images. To avoid influence from the structures around the central peak, only pixels with flux more than half of the peak are examined. Results are shown in Table 6. Except for the 2.1 and the $7.7 \mu\text{m}$ image, the FWHM of the minor axis is about $0''.2$. As noted in §3.2, deviation of the FWHM in the 2.1 and $7.7 \mu\text{m}$ image is not of the object. The FWHM in the MIR of $0''.2$ is slightly larger than the FWHM of $0''.13$ for the deconvolution test star. At all wavelengths, the central peak is elongated north and south. Hereafter, we refer the central MIR emission region of $0''.29 \times 0''.18$ as the central elliptical region. This is the FWHM fitted on the $11.7 \mu\text{m}$ image, which is made from the largest number of frames. At the distance of NGC 1068, the linear size of the central elliptical region is 21×13 pc.

Flux from the central peak is measured by applying apertures of three sizes. First, flux from the central elliptical region is measured. The result is shown in the third column of Table 1. Note that the flux at 2.1 and 7.7 μm is lower limit because of the spillover of the PSF in the deconvolved images. Second, to avoid the spillover on the 7.7 μm image, we define a larger aperture. There is a secondary peak at $0''.4$ north in the 11.7 μm image. To exclude emission from the secondary peak, the diameter of the second aperture is set to $0''.4$. The result is in the fourth column of Table 1. Figure 3 shows the measured spectral energy distributions (SEDs) in the two apertures. The silicate absorption feature at 9.7 μm is seen. Moreover, the 11.7 μm flux is larger than the 12.3 μm flux. This suggests existence of the PAH emission feature at 11.3 μm . Finally, for comparison with other observations, flux is also measured in an aperture of $4''$ diameter. The result is in the fifth column of Table 1. This can be compared with the MIR photometric observation of Rieke & Low (1975) who used a diaphragm of $4''$ diameter. Our measurement in the $4''$ aperture is about 25%–35% brighter in the 7–13 μm bands than their results. This is in reasonably good agreement considering uncertainty in the measurements and variability of the target reported in the literature. On the other hand, our measurement is about 30% less bright than their measurement around 18 μm . At the wavelength, the $4''$ diaphragm is comparable with the diffraction limit for the observations of Rieke & Low (1975). This implies that there is extended emission at around 18 μm .

4.1.2. SED Fitting

As shown by Roche et al. (1991), the absorption feature of silicate is seen in spectra of AGNs. On the other hand, PAH emission features are usually detected toward H II region galaxies. However, Voit (1992) pointed out possibility of PAH emission from an AGN if the PAH carriers are sheltered from the intense radiation. Here, the silicate absorption feature is measured with possibility of the PAH emission features taken into account.

To measure the optical depth of the silicate feature, we conduct least-squares fitting of a modified graybody radiation absorbed by the silicate feature. Integrating fitted modified graybody radiation, intrinsic luminosity of the infrared emitting media can also be estimated. Namely, SEDs in the MIR are fitted by model flux of

$$I(\lambda) = \epsilon_{\lambda_0} \left(\frac{\lambda}{\lambda_0} \right)^\alpha \times B(T_{BB}, \lambda) \times e^{-\tau_{sil}(\lambda)} \quad (1)$$

where $I(\lambda)$ is the model surface brightness at wavelength λ . The black body radiation $B(T_{BB}, \lambda)$ of temperature T_{BB} is assumed to have the emissivity and beam filling factor product, which is assumed to be ϵ_{λ_0} at λ_0 and proportional to λ^α . The modified graybody radiation is absorbed by the silicate feature of $\tau_{sil}(\lambda)$. Fitting is done on the three free parameters: T_{BB} , ϵ_{λ_0} at $\lambda_0 = 10 \mu\text{m}$, and $\tau_{9.7\mu\text{m}} = \tau_{sil}(\lambda = 9.7 \mu\text{m})$. Limited by the number of data points, α cannot be a free parameter and is fixed at -1 . For the silicate feature, we assume the “astronomical silicate” by

Laor & Draine (1993)⁴ with $0.1 \mu\text{m}$ radius. The tabulated absorption coefficient is essentially the same for dust grains with a radius smaller than $0.5 \mu\text{m}$ when normalized at $9.7 \mu\text{m}$. Mathis (1990) measured the interstellar extinction law. The result is similar to the absorption coefficient of the astronomical silicate in the MIR wavelength, but with fewer data points. As there is a possibility of contribution from PAH emission in the SEDs, we excluded the 7.7 , 8.6 , and $11.3 \mu\text{m}$ images from fitting. This also avoids influence of the PSF difference of the $7.7 \mu\text{m}$ image.

The results of least-squares fittings are shown in Table 7. Figure 3 shows the model SEDs for the central elliptical region and for the $0''.4$ aperture. For the larger aperture, the temperature is lower and the silicate absorption is shallower. The confidence map in Figure 4 shows that the background temperature and the optical depth of the silicate feature are related although, for the 1σ level, the silicate absorption exists on the SED. The results do not change much with change of the assumed power law α of emissivity and filling factor product. When α is assumed as 0 or -2 , the optical depth $\tau_{9.7\mu\text{m}}$ becomes larger or smaller, respectively, about half of its 1σ error bar, compared with the nominal value for $\alpha = 1$. Integrated graybody luminosity is 20 % larger for $\alpha = 0$ than for $\alpha = -1$. On the other hand, with $\alpha = -2$, integrated luminosity becomes 15 % smaller than that for $\alpha = -1$.

Roche et al. (1984) observed the silicate absorption feature to be $\tau_{9.7\mu\text{m}} = 0.51$ with the $4''.7$ aperture. This is consistent with our result for the $0''.4$ aperture but higher than that for the $4''$ aperture. As a consequence of deconvolution, which gathers the light into the central peak, the apertures on the deconvolved image are equivalent to larger apertures on a direct image.

4.2. PAH emission from the Central Peak

As has been pointed out, for example, by Smith, Aitken, & Roche (1989), the PAH features are associated with starburst activity. In case they are detected from the central peak, it would suggest that the PAH carriers near the AGN are sheltered from the intense radiation as proposed by Voit (1992) and that starburst activity is occurring near the AGN.

As Figure 3 shows, the observed flux is underestimated by the model at 7.7 , 8.7 , and $11.7 \mu\text{m}$, wavelengths we excluded from the fitting. Here, the excess emission is assumed to be the PAH emission features, which peak at 7.7 , 8.6 , and $11.3 \mu\text{m}$. For the $0''.29 \times 0''.18$ arcsec elliptical aperture, the $7.7 \mu\text{m}$ flux is not underestimated, because the PSF is wider than the aperture. Excess flux in the $0''.4 \phi$ aperture is 3.5 ± 1.0 , 3.5 ± 1.0 , and $2.6 \pm 1.5 \times 10^{35}$ W for the 7.7 , 8.6 , and $11.3 \mu\text{m}$ feature respectively. The contrast of the excess emission to the model continuum is higher in smaller aperture. This suggests that the PAH emission is from the central peak.

However, our result is inconsistent with other observations. Excess flux in our $4''$ aperture is

⁴Optical property available on-line at <http://www.astro.princeton.edu/~draine/>.

$L_{11.3\mu m} \sim 2 \times 10^{35}$ W. This is, for example, 7 times larger than 3.0×10^{34} W that is measured by Sturm et al. (2000) from the spectrum taken by the Short Wavelength Spectrometer on board *Infrared Space Observatory*. The single temperature continuum model adopted in this work may be too simple, and uncertainty in relative calibration between the filters may be too large to measure the excess luminosity. A spatially resolved MIR spectrum is needed to clarify whether the PAH features are emitted from the vicinity of the AGN.

4.3. Emission Structures around the Central Peak

The MIR deconvolved images show structures elongated toward two directions. In higher surface brightness, Figure 1c shows an elongation toward a P.A. of -10° from the central peak. The direction is consistent with the elongation imaged in the MIR by Bock et al. (2000). The northern part of the elongation traces the western side of the ionization cone observed by [O III] emission (Evans et al. 1991). In lower surface brightness, another structure extends wider. In the northern part, it elongates to a P.A. of 25° . This is consistent with the MIR images with wider FOV by Braatz et al. (1993) and Alloin et al. (2000). The direction of the northeastern elongation coincides with that of the jetlike structure observed by radio continua by, for example, Gallimore et al. (1996). Spatially resolved MIR spectrum may clarify the relations of the emission structures.

4.4. The Disklike Structure

In L and M bands, Marco & Alloin (2000) imaged disklike structures in east and west of the central peak. The locations are indicated by crosses in Figure 1c. The MIR emission is constricted at the locations, and essentially no MIR emission is detected.

To assess the nature of the disklike structures, SED of the disklike structures is plotted in Figure 5 with help from the NIR surface brightness taken from Marco & Alloin (2000) and Rouan et al. (1998). It is bright in the NIR but not in the MIR. The SED is compared with the model of the modified graybody emission absorbed by the silicate feature as presented by Equation (1). To attenuate the MIR emission, deep absorption of the silicate feature is needed. The absorption coefficient of the astronomical silicate and the interstellar extinction law by Mathis (1990) differs in the NIR. Therefore, we try different emission models adopting each optical parameter. When the astronomical silicate is assumed, $\tau_{9.7\mu m}$ has to be at least 10. This corresponds to a hydrogen column density N_H at least 1.6×10^{23} cm^{-2} assuming the Galactic extinction law (Roche & Aitken 1984, 1985; Predehl & Schmitt 1995). On the other hand, the model assuming the extinction law of Mathis (1990) fits reasonably with $\tau_{9.7\mu m} \sim 5$, or $N_H \sim 8 \times 10^{22}$ cm^{-2} . In the latter case K -band extinction is higher than the astronomical silicate so that the K -band brightness cannot be reproduced with $\tau_{9.7\mu m}$ higher than 5. In either case, the silicate absorption feature is too deep compared with the absorption for the central peak. Consequently, the disklike structures cannot

be explained as emission sources absorbed by dust. The nature of the disklike structures remains unclear.

5. Discussion

5.1. MIR Radiation from the Central Peak

On the $11.7 \mu\text{m}$ image, the central peak has an FWHM of $0''.29 \times 0''.18$, or a linear scale of $21 \times 13 \text{ pc}$, elongated north and south. From the direction of the [O III] cone (Evans et al. 1991), the axis of the torus is also in the north-south direction. It implies that the plausible torus has a diameter comparable or smaller than 13 pc.

Fitting on the measurement of Rieke & Low (1975), Pier & Krolik (1993) modeled emission from the AGN obscuring torus. As shown in their figure, NGC 1068 emits a considerable portion of its energy in the MIR. Thus, intrinsic luminosity of the torus can be estimated integrating the fitted modified graybody radiation. Integrating the modified graybody emission over the wavelength and surface of the ellipsoid, intrinsic luminosity of the modified graybody emission is calculated to be $3.3 \times 10^{37} \text{ W}$. This is comparable to the intrinsic X-ray emission luminosity estimated by Iwasawa et al. (1997).

5.2. Dust Absorption toward the Central Source

The measured silicate absorption is compared with observations in other wavelengths. It is known that the extinction law toward the Galactic center is different from the one for the local inter stellar matter (ISM). The measured optical depth for the central elliptical region of $\tau_{9.7\mu\text{m}} = 0.9 \pm 0.3$ corresponds to an $A_V \sim 8 \text{ mag}$ with the extinction law for the local ISM (Roche & Aitken 1984) or $17 \pm 6 \text{ mag}$ with that toward the Galactic center (Roche & Aitken 1985). The corresponding hydrogen column density is calculated as $N_{\text{H}} \sim 1.4$ or $3.0 \times 10^{22} \text{ cm}^{-2}$ (Predehl & Schmitt 1995).

As for the $3.4 \mu\text{m}$ feature of carbonaceous dust, Pendleton et al. (1994) measured the extinction law $A_V/\tau_{3.4}$ toward the Galactic center and for the local ISM. The values are again different by a factor of 2 although, optical depth ratio $\tau_{3.4\mu\text{m}}/\tau_{9.7\mu\text{m}}$ calculated from the extinction ratios only differs $\sim 20\%$. Namely, it is ~ 0.06 toward the Galactic center and ~ 0.074 for the local ISM. Using the mean value, $\tau_{9.7\mu\text{m}} \sim 0.9$ corresponds to $\tau_{3.4\mu\text{m}} \sim 0.06$. This is half of the observed optical depth (Imanishi et al. 1997). As has been suggested by Imanishi (2000), the discrepancy can be attributed to a temperature structure of the absorbing dust along the line of sight. Comparing models, the wavelength dependency of the dust features may constrain the temperature structure of dust. It should also be noted that there is evidence that the extinction law toward Seyfert nuclei is different from the one in our Galaxy throughout all wavelengths observable from the ground (Pitman,

Clayton, & Gordon 2000; Crenshaw et al. 2001; Maiolino, Marconi, & Oliva 2001a; Imanishi 2001). There is a good chance of the ratio $\tau_{3.4\mu m}/\tau_{9.7\mu m}$ being different from our Galaxy, because the difference of the extinction is attributed to different dust size distribution (Maiolino, Marconi, & Oliva 2001b; Imanishi 2001). The two possibilities, the temperature gradient and the different optical depth ratio, are not distinguishable from this work. Correlation of $\tau_{3.4\mu m}/\tau_{9.7\mu m}$ has to be investigated toward different classes of objects.

6. Conclusion

We observed the central region of the Seyfert 2 galaxy NGC 1068 using the MIRTOS on the Subaru Telescope. The oversampling pixel scale accompanied by the SAA method enables us to obtain high spatial resolution images of about $0''.13$ FWHM after Lucy-Richardson deconvolution in the MIR. The central peak of NGC 1068 in the MIR is $0''.3$ FWHM north-south and $0''.2$ FWHM east-west. It corresponds to a linear scale of 21×13 pc. With its axis has been observed to be in the north-south direction, the plausible torus has a diameter comparable or less than 13 pc. Overall structure elongates to a P.A. of -10° with another elongation of lower surface brightness at a P.A. of 20° . The six filters in the $10 \mu m$ band along with the $18.5 \mu m$ filter produced the detailed SED of the central peak. The SED of the central elliptical region of $0''.3 \times 0''.2$ is fitted to have a modified graybody emission of 234 K with silicate absorption feature $\tau_{9.7\mu m} = 0.9 \pm 0.3$. Intrinsic luminosity of the central peak is about 3×10^{37} W. The MIR silicate absorption feature is half of that estimated from the NIR spectroscopy (Imanishi et al. 1997) when the Galactic extinction law is assumed. This can be explained by a temperature gradient of dust along the line of sight as Imanishi (2000) suggested, or by different dust-size distribution as Maiolino et al. (2001b) and Imanishi (2001) pointed out. From the central source, there is excess emission at the wavelengths of the PAH emission features. Uncertainty of the measurement is huge, and we have to wait for a high spatial resolution spectrum. However, this suggests that the PAH carrier is shielded from high energy radiation from the AGN (Voit 1992) and the existence of the nuclear starburst. No MIR emission is detected as counterparts for the NIR disklike structures (Alloin et al. 2000). The nature of the structure is still unclear.

We are grateful to Danielle Alloin for valuable suggestions during her stay at National Astronomical Observatory of Japan in Tokyo, Japan. We thank Naoto Kobayashi and Masayuki Akiyama for many constructive discussions. Also, we thank Masatoshi Imanishi and the anonymous referee who suggested us many viewpoints to investigate our data. The staff at the Subaru Telescope enabled to realize the observations with the newly constructed instrument. We appreciate their enormous efforts. D. T. has been supported by the Research Fellowship for Young Scientists from the Japan Society for the Promotion of Science.

REFERENCES

- Alloin, J., et al. 2000, *A&A*, 363, 926
- Antonucci, R. 1993, *ARA&A*, 31, 473
- Antonucci, R. & Miller, J. S. 1985, *ApJ*, 297, 621
- Bock, J. J., et al. 2000, *AJ*, 120, 2904
- Bottinelli, L., et al. 1990, *A&AS*, 82, 391
- Braatz, J. A., et al. 1993, *ApJ*, 409, L5
- Cohen, M., et al. 1995, *AJ*, 110, 275
- Cornwell, T. J. & Evans, K. F. 1985, *A&A*, 143, 77
- Crenshaw, D. M., Kraemer, S. B., Bruhweiler, F. C., & Ruiz, J. R. 2001, *ApJ*, 555, 633
- Elias, J. H., et al. 1982, *AJ*, 87, 1029
- Evans, I. N., et al. 1991, *ApJ*, 369, L27
- Gallimore, J. F., Baum, S. A., & O’Dea, C. P. 1996, *ApJ*, 464, 198
- Imanishi, M. 2000, *MNRAS*, 319, 331
- Imanishi, M. 2001, *AJ*, 121, 1927
- Imanishi, M., et al. 1997, *PASJ*, 49, 69
- Iwasawa, K., et al. 1997, *MNRAS*, 289, 443
- Laor, A. & Draine, B. T. 1993, *ApJ*, 402, 441
- Lucy, L. B. 1974, *AJ*, 79, 745
- Maiolino, R., Marconi, A., & Oliva, E. 2001a, *A&A*, 365, 28
- Maiolino, R., Marconi, A., & Oliva, E. 2001b, *A&A*, 365, 37
- Marco, O. & Alloin, D. 2000, *A&A*, 353, 465
- Marco, O., Alloin, D., & Beuzit, J. L. 1997, *A&A*, 320, 399
- Mathis, J. S. 1990, *ARA&A*, 28, 37
- Pendleton, Y. J., Sandford, S. A., Allamandola, L. J., Tielens, A. G. G. M., & Sellgren, K. 1994, *ApJ*, 437, 683

- Pier, E. A. & Krolik, J. H. 1993, *ApJ*, 418, 673
- Pitman, K. M., Clayton, G. C., & Gordon, K. D. 2000, *PASP*, 112, 537
- Predehl, P. & Schmitt, J. H. M. M. 1995, *A&A*, 293, 889
- Rieke, G. H., et al. 1984, *AJ*, 90, 900
- Rieke, G. H. & Low, F. J. 1975, *ApJ*, 199, L13
- Roche, P. F. & Aitken, D. K. 1984, *MNRAS*, 208, 481
- Roche, P. F. & Aitken, D. K. 1985, *MNRAS*, 215, 425
- Roche, P. F., Aitken, D. K., Phillips, M. M., & Whitmore, B. 1984, *MNRAS*, 207, 35
- Roche, P. F., Aitken, D. K., Smith, C. H., & Martin, J. W. 1991, *MNRAS*, 248, 606
- Rouan, D., et al. 1998, *A&A*, 339, 687
- Smith, C. H., Aitken, D. K., & Roche, P. F. 1989, *MNRAS*, 241, 425
- Sturm, E., et al. 2000, *A&A*, 358, 481
- Tokunaga, A. T. 1984, *AJ*, 89, 172
- Tomono, D. 2000, Ph. D. thesis, Univ. Tokyo
- Tomono, D., Doi, Y., & Nishimura, T. 2000, *Proc. SPIE*, 4008, 853
- Voit, G. M. 1992, *MNRAS*, 258, 841

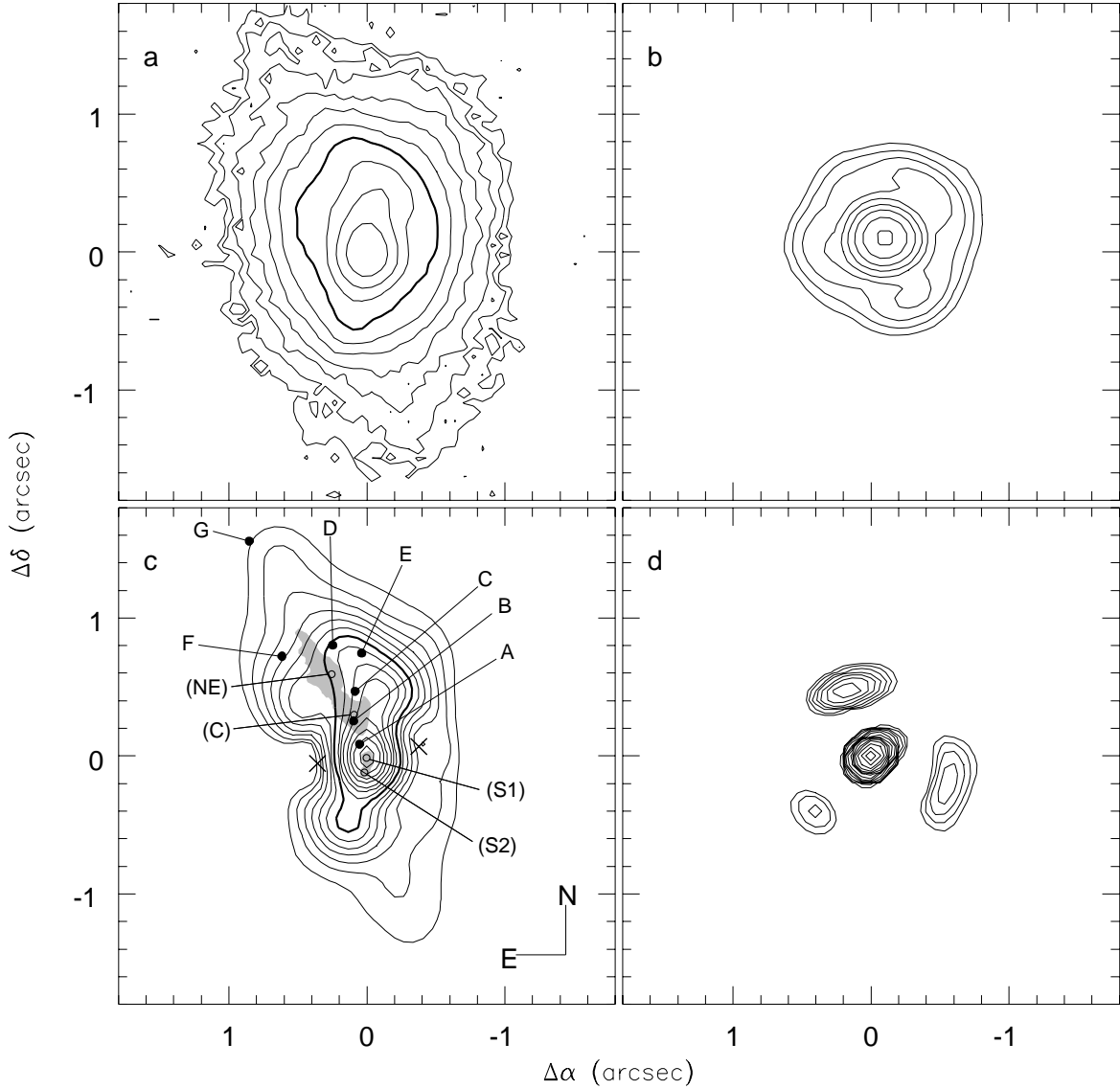


Fig. 1.— Contour maps of NGC 1068 at $11.7 \mu\text{m}$. (a) The SAA image with contours starting at $0.63 \text{ Jy arcsec}^{-2}$, which is the 3σ level. The PSF reference image used for the Lucy-Richardson deconvolution is shown in (b). (c) The image of NGC 1068 after deconvolution. (d) The image of the test point source deconvolved with the same PSF reference. Five contours are plotted for a decade of surface brightness in a logarithmic scale. The thick contour is $10 \text{ Jy arcsec}^{-2}$ in (a) and (c). The filled circles in (c) show the locations and the names of the [O III] emitting clouds (Evans et al. 1991). Crosses are the locations of the M-band disklike structures (Marco & Alloin 2000). Gray shade and open circles show the locations and the names of the 5 GHz continuum emission (Gallimore, Baum, & O’Dea 1996).

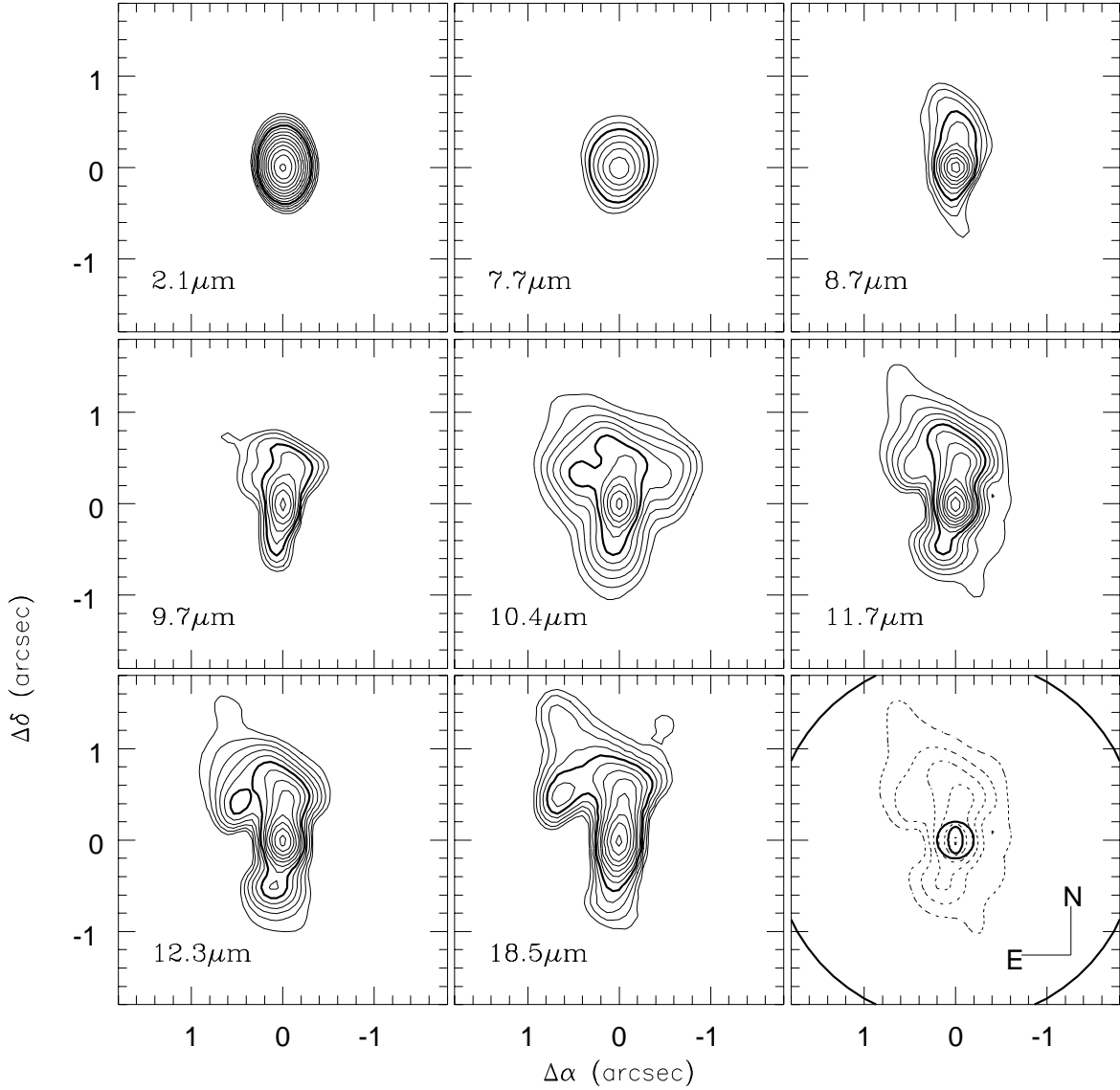


Fig. 2.— Deconvolved images of NGC 1068. Contours start above the 3σ noise level. Five contours are spaced equally in a logarithmic scale in a decade. The 10 Jy arcsec⁻² (0.1 Jy arcsec⁻² for the 2.1 μm image) contours are plotted with thick lines. The lower right-hand panel shows the apertures used for SED measurements overlaid on the 11.7 μm image.

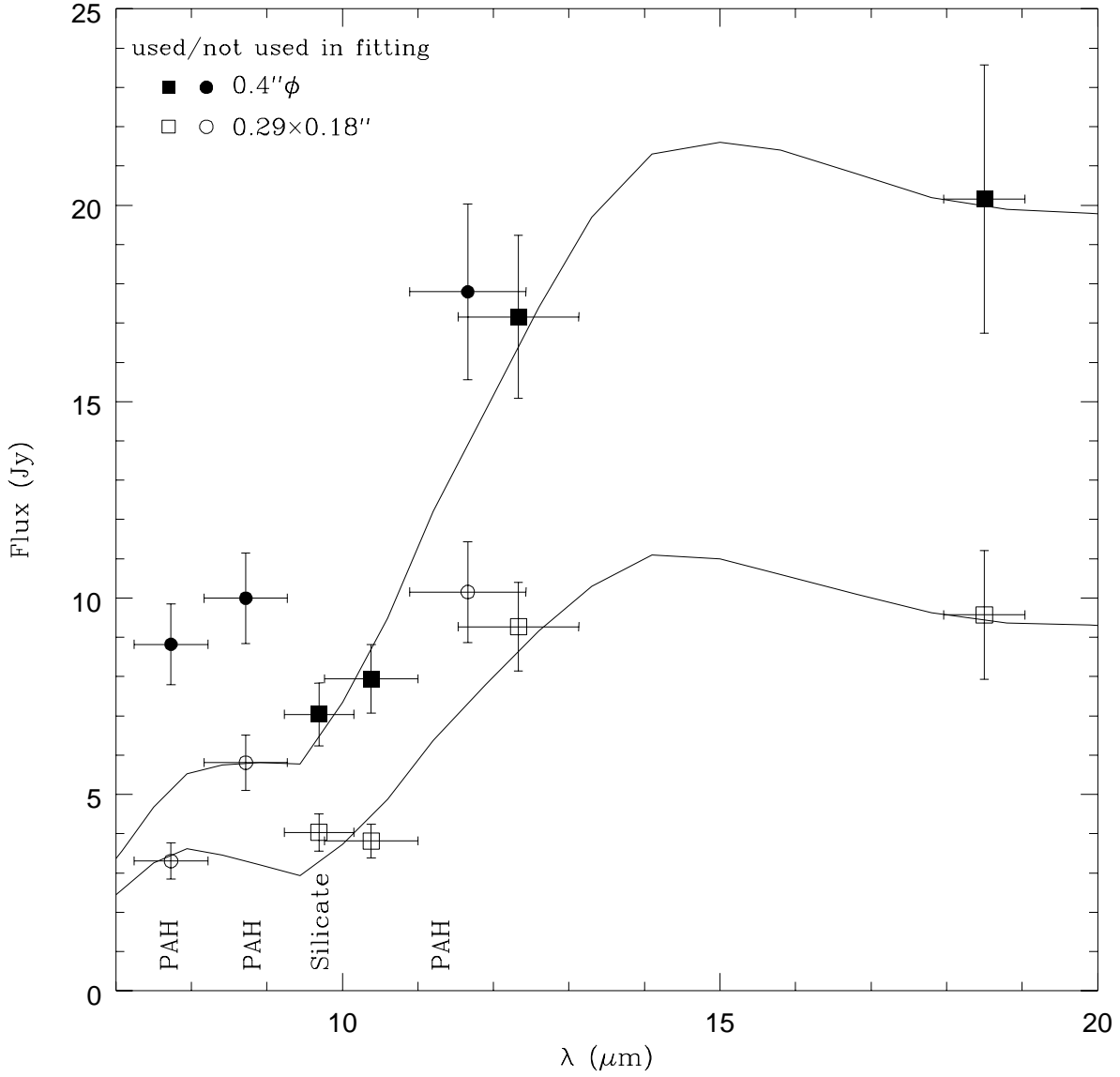


Fig. 3.— Flux in the apertures on the deconvolved images. The filled symbols show flux within the $0''.4$ aperture. The open symbols show flux within the central elliptical region of $0''.29 \times 0''.18$. The upper curve shows the best-fit model for the $0''.4$ aperture. The lower curve shows the best-fit model for the $0''.29 \times 0''.18$ aperture. Flux at 7.7 , 8.7 , and $11.7 \mu\text{m}$, which is shown with circles, is not used in fitting owing to the possibility of PAH emission. Best-fit parameters are shown in Table 7. Wavelengths of peaks of the silicate features and the PAH features are also shown.

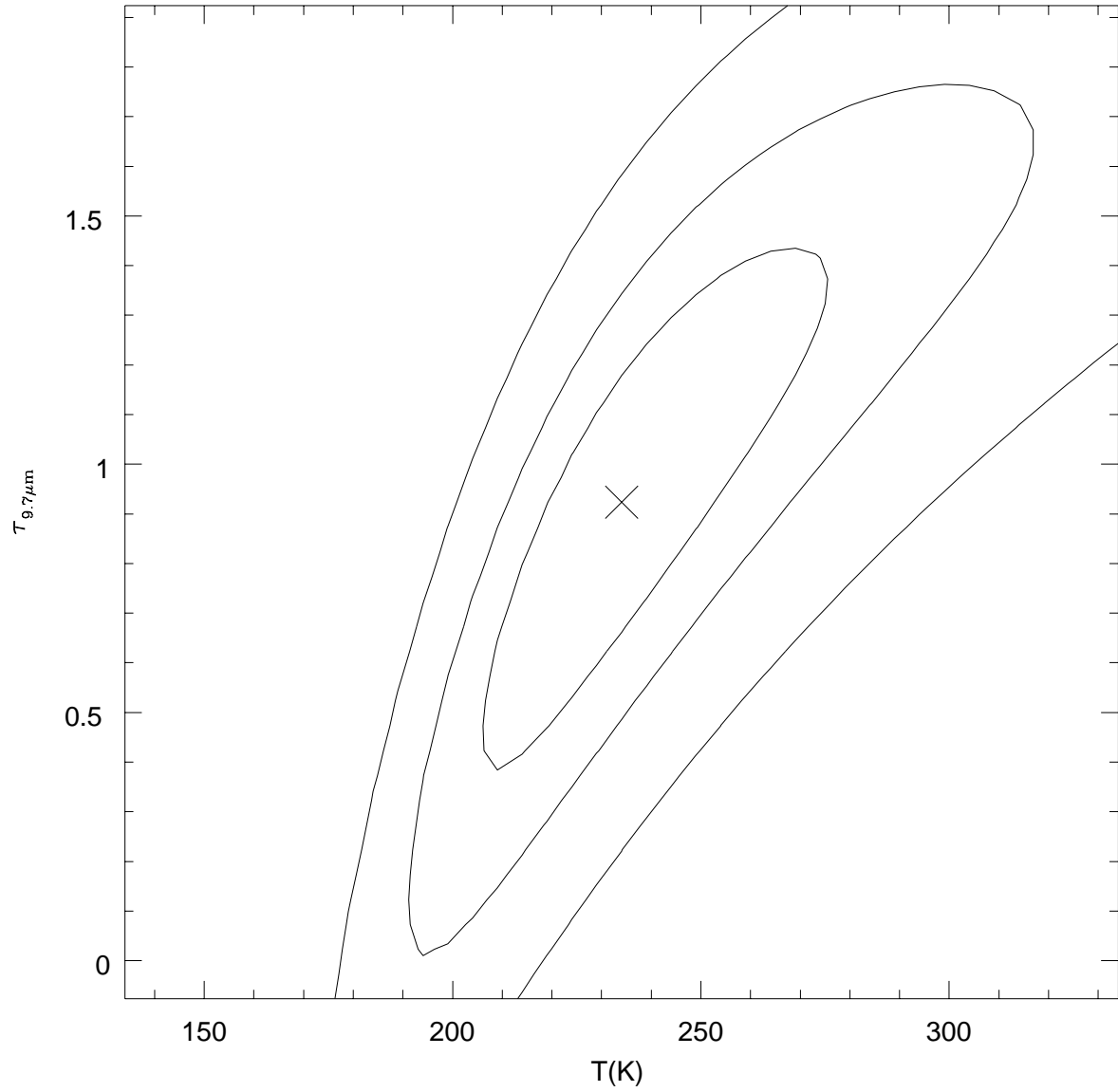


Fig. 4.— Confidence map of least-squares fitting on the SED for the $0''.29 \times 0''.18$ aperture. Contours are for confidence levels of 68.3 % (1σ), 90 %, and 99 %.

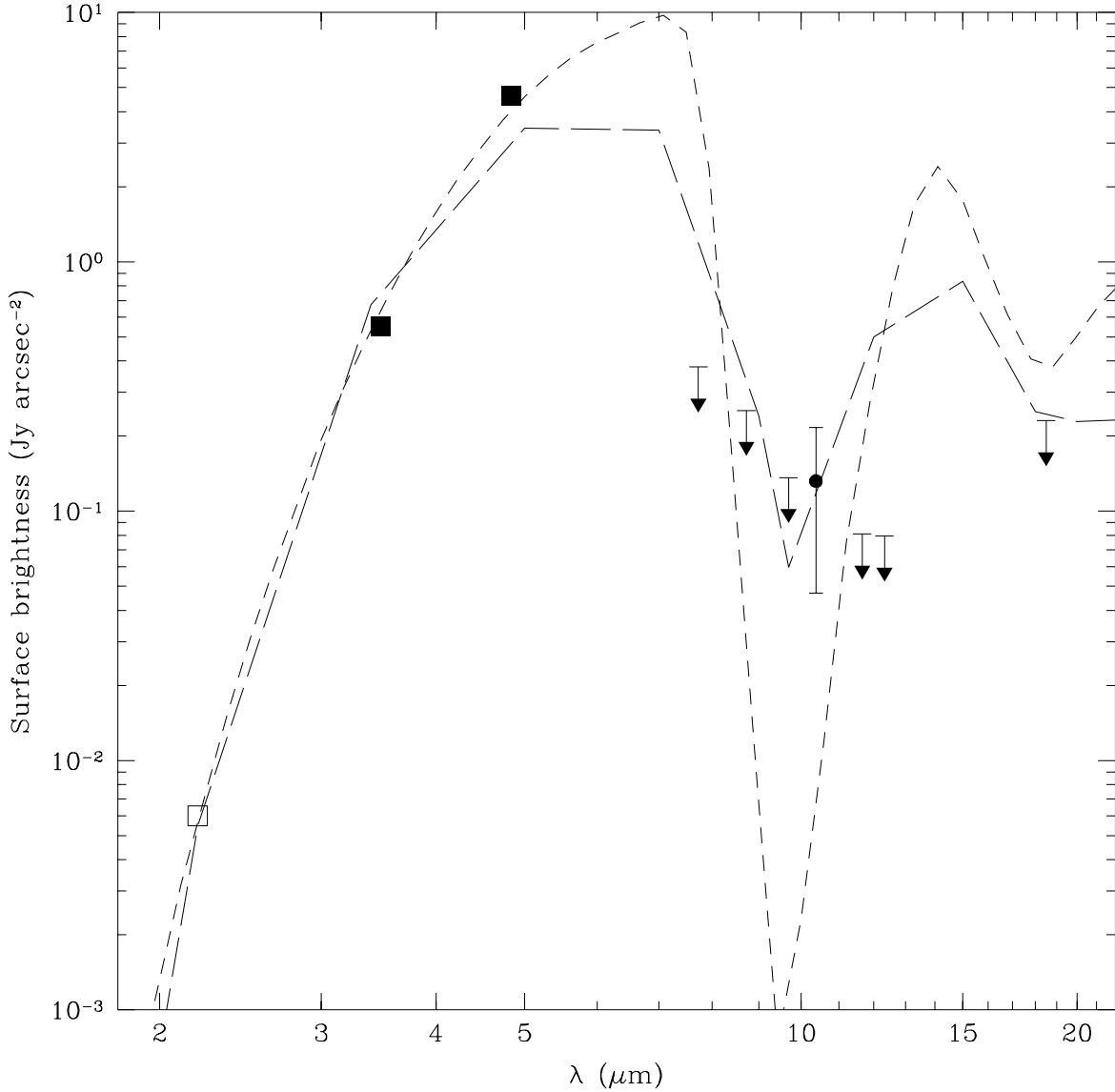


Fig. 5.— Average SED of the disklike structures in the east and the west of the central peak imaged by Marco & Alloin (2000). The filled squares are taken from Marco & Alloin (2000). The K -band brightness taken from Rouan et al. (1998) is shown with an open square. No emission is detected in the MIR images. Upper limits of the 1σ level are shown. Curves show the models of modified graybody emission absorbed by the silicate feature. The short-dashed curve shows the model with 390 K background emission absorbed by astronomical silicate (Laor & Draine 1993) with $\tau_{9.7\mu m} = 10$. The long-dashed curve shows the model with 1360 K background emission and the extinction law by Mathis (1990) with $\tau_{9.7\mu m} = 5$.

Table 1. Filter Path Bands and Observed Flux of NGC 1068 in Apertures on Images Deconvolved by the Lucy-Richardson Algorithm

λ (μm)	$\Delta\lambda$ (μm)	$0''.29 \times 0''.18^{\text{a}}$ (Jy)	$0''.4 \phi$ (Jy)	$4''\phi$ (Jy)
2.12	0.36	$0.218 \pm 0.027^{\text{b}}$	$0.432 \pm 0.054^{\text{b}}$	0.560 ± 0.070
7.73	0.70	$3.31 \pm 0.46^{\text{b}}$	8.8 ± 1.0	16.2 ± 1.9
8.72	0.78	5.81 ± 0.70	10.0 ± 1.2	16.5 ± 1.9
9.69	0.94	4.03 ± 0.48	7.04 ± 0.80	16.1 ± 1.8
10.38	1.02	3.82 ± 0.43	7.94 ± 0.87	22.8 ± 2.5
11.66	1.16	10.2 ± 1.3	17.8 ± 2.2	33.9 ± 4.3
12.33	1.18	9.3 ± 1.1	17.2 ± 2.1	33.3 ± 4.0
18.50	1.08	9.6 ± 1.6	20.2 ± 3.4	46.6 ± 7.9

Note. — Error bars include uncertainty in the conversion factors.

^aEllipse with P.A. of 0° .

^bThe values are lower limits because the PSF is larger than the aperture.

Table 2. Number of Observed Nodding Sets for NGC 1068

UT	2.1 μm	7.7 μm	8.7 μm	9.7 μm	10.4 μm	11.7 μm	12.3 μm	18.5 μm
Dec 31	4	8
Jan 9	24	2	2	2	4	4	6	4
Jan 18	22	8	12	12

Note. — One nodding set corresponds to 3 s of integration time on-source.

Table 3. Number of Observed Nodding Sets for PSF Reference Stars

UT	2.1 μm	7.7 μm	8.7 μm	9.7 μm	10.4 μm	11.7 μm	12.3 μm	18.5 μm
Dec 31	2 ^a	2 ^a
Jan 9	2 ^b	2 ^c	2 ^c	2 ^c	6 ^c	2 ^c	2 ^c	...
Jan 18	4 ^d	2 ^e	2 ^e	4 ^e

^a α Ari.

^bHD 40335.

^c α CMa.

^dGJ 105.5.

^e β And.

Table 4. Number of Observed Nodding Sets for Deconvolution Test Stars

UT	2.1 μm	10.4 μm	11.7 μm	18.5 μm
Dec 31	...	2 ^a	2 ^a	4 ^a
Jan 9	2 ^b	...	5 ^a	...

^a β And.

^bGJ 105.5.

Table 5. Number of Observed Nodding Sets for Flux Reference Stars

UT	2.1 μm	7.7 μm	8.7 μm	9.7 μm	10.4 μm	11.7 μm	12.3 μm	18.5 μm
Dec 31	4 ^a + 2 ^b	28 ^a + 26 ^b
Jan 10	54 ^c + 12 ^d	2 ^b + 2 ^e	2 ^b + 8 ^e	2 ^b + 4 ^e	2 ^b + 14 ^e	28 ^b + 14 ^e	2 ^b + 2 ^e	4 ^b
Jan 19	6 ^c	12 ^b	2 ^b	6 ^b

^a α Ari.

^b β And.

^cGJ 105.5.

^dHD 40335.

^e α CMa.

Table 6. FWHM of the Central Peak after Lucy-Richardson Deconvolution

λ (μm)	Major axis (arcsec)	Minor axis (arcsec)	P.A. of major axis (degrees)	Reference ^a (arcsec)
2.1	0.74	0.54	+0.6	0.48
7.7	0.36	0.33	+0.0	...
8.7	0.26	0.21	+1.2	...
9.7	0.39	0.21	+0.1	...
10.4	0.35	0.23	-0.6	0.11
11.7	0.29	0.18	+0.6	0.13
12.3	0.30	0.19	+0.2	...
18.5	0.43	0.22	+0.2	...

^aFWHM of the deconvolution test star after Lucy-Richardson deconvolution.

Table 7. Best-Fit Parameters on Central Peak

Aperture arcsec	T_{BB} K	$\tau_{9.7\mu m}$	$\log_{10}(\epsilon_{10\mu m})$	χ^2
0.29×0.18 ellipse	234 ± 22	0.92 ± 0.34	-0.98 ± 0.14	5.1
0.4ϕ	219 ± 19	0.72 ± 0.33	-1.06 ± 0.14	1.5
4ϕ	201 ± 15	0.12 ± 0.30	-2.64 ± 0.14	0.4

Note. — Blackbody radiation is assumed to have emissivity and filling factor product proportional to λ^{-1} . SEDs are fitted with the three free parameters on flux at 9.7, 10.4, 12.3, and 18.5 μm .